CrystEngComm

PAPER

Check for updates

Creating supramolecular semiregular Archimedean tilings *via* gas-mediated deprotonation of a terminal alkyne derivative†

Wenqi Hu,[ab] Hexu Zhang,[ab] Peng Cheng,[ab] Lan Chen, [iD][ab] Zhi Chen, [iD][c]
Svetlana Klyatskaya,[c] Mario Ruben,*[cde] Johannes V. Barth,*[f]
Kehui Wu*[ab] and Yi-Qi Zhang [iD] *[a]

Combining surface-confined reactions with supramolecular self-assembly allows the chemical transformation of simple molecular precursors into higher-level tectons to generate complex tessellations with unique structural and functional properties. Herein, utilizing low-temperature scanning tunnelling microscopy, we firstly confirm a highly efficient chemical reaction converting ethynyl-phenanthrene (EP) precursors into bis(phenanthren-2-yleythnyl)silver (BPE–Ag) complexes adsorbed on Ag(111)/mica at room temperature *via* a novel oxygen-gas mediated terminal alkyne deprotonation process. Moreover, we show that the BPE–Ag species engage in the formation of three distinct types of long-range ordered nanoporous supramolecular architectures, which can be tuned by the initial EP coverage. For all three phases, the basic tectons were verified to be BPE–Ag dimers with flexible pairing configurations. Intriguingly, our tiling analysis reveals that two phases belong to the (3.6.3.6) class of semiregular Archimedean tiling (AT) and the third expresses a new (3.4.6.4) AT, different from the previously reported related networks. Our results illustrate the potential of the introduced synthesis strategy towards accessing architectures with increased complexity and pave the way towards further control and exploration regarding functional properties of interfacial semiregular ATs.

Introduction

Archimedean tilings (ATs) refer to eleven distinct types of periodic two-dimensional (2D) nets, in which regular polygons are arranged in an edge-to-edge fashion whereby the vertices of the tiling belong to the same type. ATs can be further divided into regular and semiregular nets depending on whether they consist of one or the combination of several regular polygons.[1–3] Recently, ATs have been receiving

*[a] Institute of Physics, Chinese Academy of Sciences, Beijing 100190, China.
E-mail: khwu@iphy.ac.cn, yiqi.zhang@iphy.ac.cn*
[b] School of Physical Sciences, University of Chinese Academy of Sciences, Beijing 100049, China
[c] Institute of Nanotechnology, Karlsruhe Institute of Technology, 76344 Eggenstein-Leopoldshafen, Germany. E-mail: mario.ruben@kit.edu
[d] Institute for Quantum Materials and Technologies (IQMT), Karlsruhe Institute of Technology (KIT), Hermann-von-Helmholtz-Platz 1, 76344, Eggenstein-Leopoldshafen, Germany
[e] Centre Européen de Sciences Quantiques (CESQ), Institut de Science et d'Ingénierie Supramoléculaires (ISIS), 8 allée Gaspard Monge, BP 70028, 67083 Strasbourg Cedex, France
[f] Physics Department E20, Technical University of Munich, D-85748 Garching, Germany. E-mail: jvb@tum.de
† Electronic supplementary information (ESI) available. See DOI: 10.1039/d1ce01413g

renewed interests in connection with the rapidly growing field of 2D materials,[4,5] as the planar crystallographic orders are usually governed by ATs. Although many theoretical studies had shown that 2D lattices featuring semiregular ATs present remarkable chemical and physical properties,[6–15] inorganic compounds featuring semiregular ATs turned out to be few.[16,17] Alternatively, engineering 2D supramolecular crystals[18–21] provides a practical way to access semiregular ATs,[22–26] opening up new avenues towards further exploiting their unique functional properties.

Recently, we introduced a methodology combining interfacial chemical reactions[27–29] with molecular self-assembly on a well-defined metal crystal lattice under ultrahigh vacuum (UHV) conditions to achieve a supramolecular (3.4.6.4) AT structure employing the simple dissymmetric precursor ethynyl-iodophenanthrene (EIP).[30] *Via* a multi-step convergent reaction pathway on Ag(111), EIP molecules were transformed into the organometallic complex bis(phenanthren-2-yleythnyl)silver (BPE–Ag) with high yield, and the geometrically flexible building blocks afford the rare (3.4.6.4) AT.[30] Both scanning tunnelling microscopy (STM) and X-ray photoelectron spectroscopy (XPS) investigations showed that the iodine atoms cleaved from the EIP molecules remained on the Ag(111) surface and are embedded in the supramolecular architecture. However, it still remains unclear whether these iodine atoms are the essential

ingredients to form the (3.4.6.4) AT. In subsequent work exploring on-surface chemistry of alkyne derivatives,[31] we revealed that the alkynyl–Ag–alkynyl bond can also be obtained *via* an O_2-gas mediated terminal alkyne deprotonation process on Ag(111).[32] This protocol provides an alternative route to synthesize regular organometallic networks[33–37] using precursors free from halogen atoms.

In order to extend the scope of current fabrication protocols, herein we introduce a two-step synthesis of BPE–Ag complexes on Ag(111)/mica employing the halogen-free ethynyl-phenanthrene (EP) precursor. We found that *via* O_2-treatment of EP molecules adsorbed on Ag(111)/mica held at room temperature (RT), the BPE–Ag species can be directly generated with high yield (>92%), which indicates that this approach is applicable to a variety of alkyne derivatives. Furthermore, *via* controlling the initial EP coverage, three distinct types of porous networks can be generated from BPE–Ag species. Based on low-temperature scanning tunnelling microscopy (LT-STM) observations, the basic building blocks for all three phases are assigned to organometallic BPE–Ag dimers, adopting versatile geometrical configurations for

pairing. Tiling analysis reveals that two of the nanoporous phases belong to the (3.6.3.6) AT, namely, the Kagome tiling, whereas the third phase expresses the rare (3.4.6.4) AT. Remarkably, the halogen-free (3.4.6.4) AT is reminiscent of the iodine-atom-incorporated (3.4.6.4) AT network reported earlier.[30] The respective major differences are associated with the basic building blocks, whereby the BPE–Ag species tend to form dimeric arrangements without the presence of iodine atoms on the surface. Thus our results enhance potential of the introduced fabrication schemes, wherein supramolecular architectures with increasing complexity are accessed *via* chemically converting functional molecular species into higher-level tectons.

Results and discussion

Oxygen-gas-mediated formation of BPE–Ag species

After depositing a small amount of EP molecules onto the Ag(111)/mica substrate held at room temperature (RT), a prevailing distribution of discrete trimeric EP clusters was observed by STM (*cf.* green circles in Fig. S1a†). The chiral three-
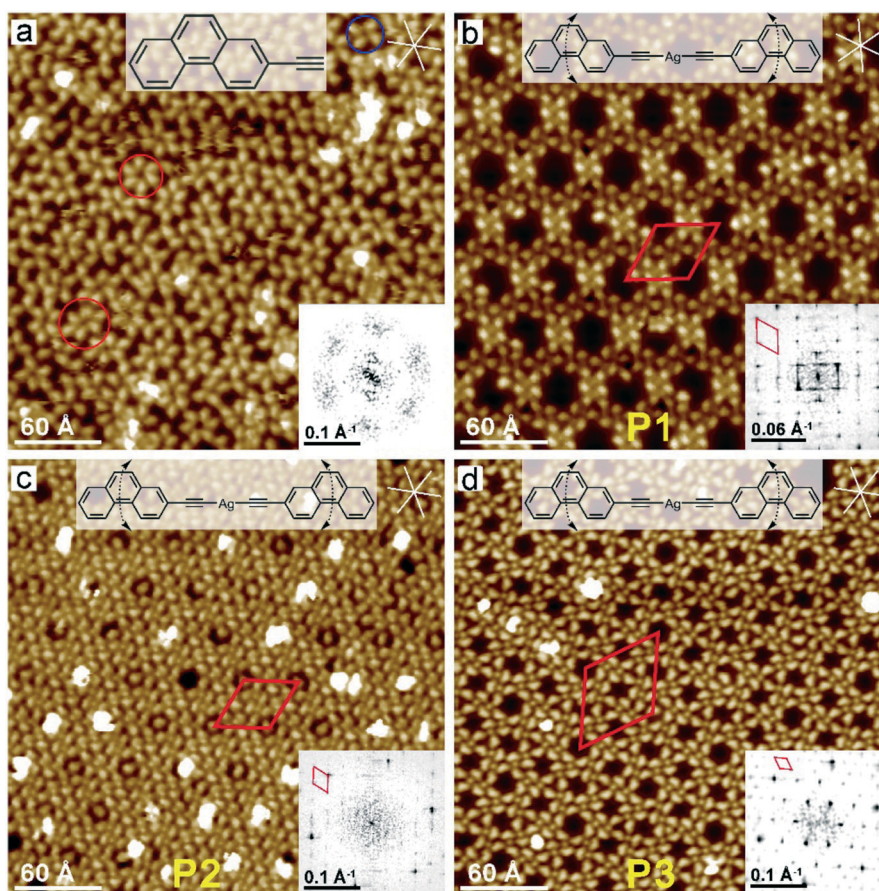

Fig. 1 (a) Large-scale STM image of intact EP molecular grown on Ag(111)/mica at RT. I_t = 50 pA, U_s = 1.0 V. Isolated tetramers and hexamers are highlighted by blue and red circles, respectively. Large-scale STM images of three different types of porous phases: (b) phase P1, (c) phase P2, and (d) phase P3, consisting of BPE–Ag species. Chemical structures of the building block for each phase are displayed as inset and the bottom right inset in each figure corresponds to the 2D fast Fourier transform (2D-FFT) of each image. Red rhombus indicates unit cell in the real and reciprocal space, respectively. High-symmetry directions of the Ag(111) surface are indicated. Scanning parameters for each image are: (b) I_t = 30 pA, U_s = 1.0 V; (c) I_t = 30 pA, U_s = 1.0 V; (d) I_t = 30 pA, U_s = 1.0 V.

fold bonding motifs (Fig. S1a and b†) were previously reported in supramolecular assemblies of different types of alkyne derivatives,[30,38,39] which can be ascribed to the weak C–H⋯π interaction[40] between terminal alkynes (*cf.* Fig. S1a and b†). With increasing EP coverage, larger clusters comprising four to six molecules (*cf.* blue and red circles in Fig. 1a and S1c†) became dominant on the surface. The molecular arrangements in clusters of different sizes were assessed *via* a simplified density functional theory (DFT) modelling, describing EP molecules in the gas-phase (*cf.* Fig. S1†), overall supporting the data interpretation. Therefore, we conclude that the EP molecules remain intact after RT deposition.

In our previous study,[32] we showed that exposing adsorbed intact terminal alkynes on Ag(111) to gaseous dioxygen in a temperature range between 200 K to 300 K triggers an effective alkyne deprotonation process, leading to the formation of alkynyl–Ag–alkynyl bond under moderate conditions (temperature range from 250 K to 375 K). To test whether this reaction scheme is effective for other terminal alkyne derivatives, we applied the same recipe to samples of different EP coverage, while keeping the substrate at RT during O₂ dosage, following which the samples were subsequently transferred to the STM chamber for examination. Notably, discrete clustered supramolecular assemblies were found to transform into long-range ordered domains. After carrying out multiple trials, overall three different types of nanoporous phases (denoted by P1, P2 and P3; *cf.* Fig. 1 and S2†) could be determined and each phase can be selectively reproduced *via* controlling the initial EP coverage. The crystallinity of each phase is confirmed *via* two-dimensional fast Fourier transformation (2D-FFT) of the extended single domains depicted in Fig. 1b–d, whereby well-defined periodic reciprocal lattices can be seen. Upon careful scrutiny, it is recognized that, apart from small amount of trapped species in the pores, the entities constituting all networks types correspond to BPE–Ag complexes (*cf.* Scheme 1). This clearly indicates that the EP

molecules underwent chemical transformations, as explained by the reaction pathway proposed in Scheme 1.

Similar to the reaction scheme identified previously,[32] the molecular O₂ efficiently deprotonates terminal alkyne groups of EP molecules adsorbed on Ag(111)/mica at RT and subsequently, two alkynyl groups presenting radical sites bind to Ag adatom thermally released from the silver substrate, and as a consequence the alkynyl–Ag–alkynyl bond forms. Uncovered Ag(111)/mica surface area was examined by STM after dosing O₂ gas and we did not observe any noticeable surface defects such as dark holes, which could indicate the presence of oxygen atoms.[41,42] Therefore, we assume that chemisorbed oxygen species was not generated on Ag(111)/mica substrate held at RT (*cf.* also Methods), agreeing with our previous study.[32] It is worth noting that the same BPE–Ag complex is the basic building block of the previously reported semiregular (3.4.6.4) AT.[30] However, the (3.4.6.4) AT encountered earlier was not reproducible for samples with different molecular density, which suggests that the missing element in the present experiments, namely the iodine atoms, plays an important role in the supramolecular organization.

Kagome phase 1 (P1)

The individual molecular entity in the supramolecular phase P1 features a dissymmetric dumb-bell shape, which can be discerned either as the *trans* or as the *cis* BPE–Ag conformers in the high-resolution STM images (*cf.* red and blue outlines in Fig. 2a and c). For a quick assessment of structural characteristics of the P1 phase, each BPE–Ag molecule is abstracted by a rod, whose colour specifies its in-plane orientation (Fig. 2a). It is clear to see that all the BPE–Ag species in the porous network are paired and each nanopore (size ≈ 470.00 Å²) in P1 is enclosed by six BPE–Ag dimers with chiral organization and both ends of each BPE–Ag pair are involved in two neighbouring nanocavities. Moreover, three chirally organized BPE–Ag complexes confine a small triangular pore (*cf.* white triangle in Fig. 2a). Next, we extract the unit cell parameters of the P1 phase (*cf.* Methods). Two primitive translation vectors of the supramolecular network P1 are defined as $\vec{a}_{P1}$ and $\vec{b}_{P1}$, which connects the centres of the neighbouring nanopores along two different directions, respectively. The experimentally determined values for the unit cell of P1 phase are $|\vec{a}'_{P1}| = 44.6 \pm 0.2$ Å, $|\vec{b}'_{P1}| = 44.8 \pm 0.3$ Å, and $\alpha'_{P1} = 60.1 \pm 0.1°$ (*cf.* Fig. 2b). The angle γ'_{P1} between $\vec{b}'_{P1}$ and one of the [Ī10] high-symmetry directions (horizontal direction in Fig. 2b) is 33.8 ± 0.1°. Guided by the experimental values and assuming a commensurate unit cell with respect to the underlying substrate lattice, the elementary cell can be written in matrix representation[43] as:

$$\begin{pmatrix} \vec{a}_{P1} \\ \vec{b}_{P1} \end{pmatrix} = \begin{pmatrix} 18 & 10 \\ -10 & 8 \end{pmatrix} \begin{pmatrix} \vec{u} \\ \vec{v} \end{pmatrix},$$

where $\vec{u}$ and $\vec{v}$ are the primitive vectors of the Ag(111) surface (Fig. 2b). With the nearest-neighbour distance $a_0 = |\vec{u}| = |\vec{v}| =$
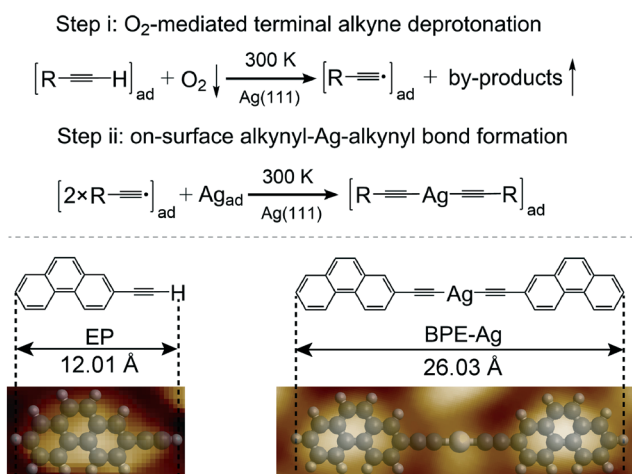
Scheme 1 Two-step synthesis of BPE–Ag species *via* oxygen-gas mediated deprotonation of terminal alkynes on the Ag(111)/mica surface. Typical STM appearance of EP and BPE–Ag species superimposed with scaled models.
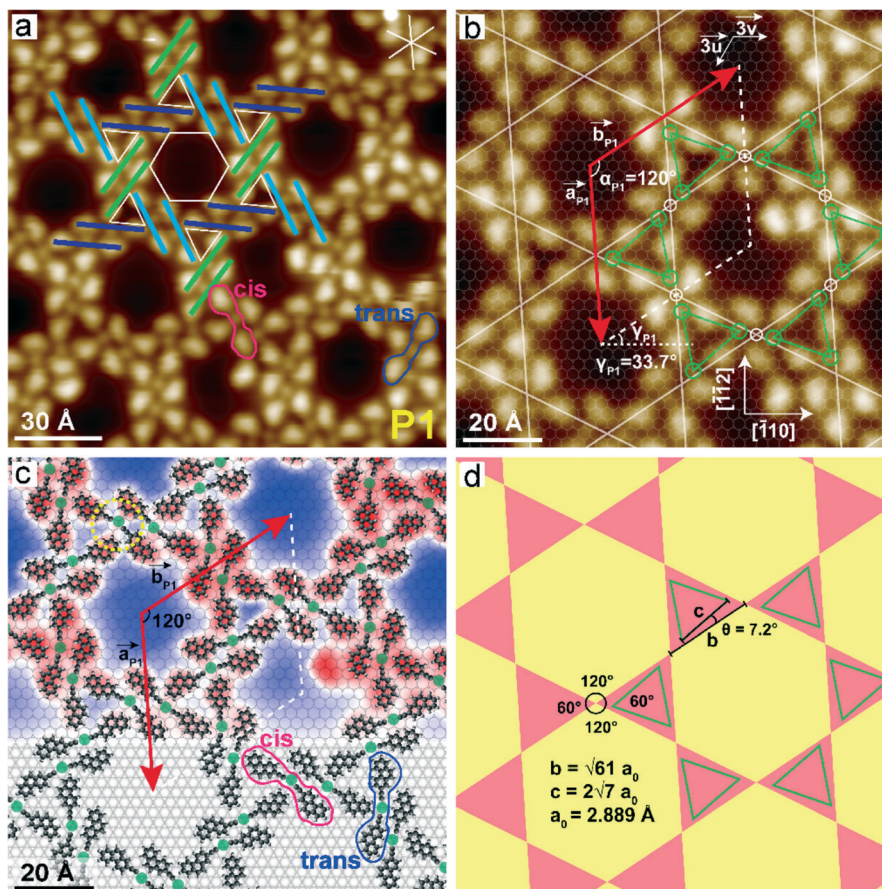
Step i: O₂-mediated terminal alkyne deprotonation

$$[\text{R}\!-\!\!\!\equiv\!\!\!-\text{H}]_{ad} + \text{O}_2 \xrightarrow[\text{Ag(111)}]{300\text{ K}} [\text{R}\!-\!\!\!\equiv\!\!\cdot]_{ad} + \text{by-products}\uparrow$$

Step ii: on-surface alkynyl-Ag-alkynyl bond formation

$$[2\times\text{R}\!-\!\!\!\equiv\!\!\cdot]_{ad} + \text{Ag}_{ad} \xrightarrow[\text{Ag(111)}]{300\text{ K}} [\text{R}\!-\!\!\!\equiv\!\!\!-\text{Ag}\!-\!\!\!\equiv\!\!\!-\text{R}]_{ad}$$

EP
12.01 Å

BPE-Ag
26.03 Å

Fig. 2 Molecular-level expression of the P1 phase. (a) High-resolution STM image for the λ-domain of P1. Each BPE–Ag species is abstracted by a straight line whose colour corresponds to its in-plane direction. The white hexagon and triangles highlight the nanopore enclosed by the BPE–Ag molecules. The *cis* and *trans* conformers of BPE–Ag are highlighted with red and blue outlines, respectively. I_t = 30 pA, U_s = 1.0 V. (b) Magnified STM image of (a) with a commensurate unit cell and proposed registry superimposed. Green circles highlight alkynyl–Ag nodes, whereas the white circles defined at the midpoints of the BPE–Ag pair give rise to the Kagome (3.6.3.6) AT. (c) STM image of (b) superposed with molecular registry. The yellow dashed circle highlights the bonding motif. (d) Tiling representation of (b) with geometric parameters.

2.889 Å of Ag(111), we obtain $|\vec{a}_{P1}| = |\vec{b}_{P1}| = 2\sqrt{61}\ a_0 = 45.13$ Å, $\alpha_{P1} = 60°$, and $\gamma_{P1} = 33.7°$. A nice agreement has been reached between the model and the experimental findings within an error smaller than 1.2%. For the P1 phase, there are six BPE–Ag molecules in each unit cell, and thus the molecular density of P1 can be deduced as η_{P1} = 0.68 molecule per nm^2 assuming an empty pore. Statistical analysis reveals that the initial EP coverage for obtaining P1 phase is around 0.65 molecule per nm^2, which is comparable to η_{P1}. Note that EP molecule is the smallest unit for density calculation, and the same criterion has been adopted for evaluating the other two phases.

To obtain the molecular adsorption registry for P1, a high-resolution STM image of the P1 phase (*cf.* Fig. 2c) is superimposed with silver lattice and each half of BPE–Ag complex was fitted with a scaled ball-and-stick model of deprotonated EP molecule relaxed by DFT methods (*cf.* Methods), and the alkynyl silver atom was not taken into account in the calculation and is simply illustrated using a circle, such that we gained more flexibility to match the *cis*

and *trans* conformers as well as the small curvature existing in the alkynyl–Ag–alkynyl bond. Interestingly, both *cis* (red outline) and *trans* (blue outline) conformers of the organometallic building block are present within one domain without showing any ordering systematics,[30] which will be discussed later in details. A slight geometrical bending of BPE–Ag (Fig. 2c) is present and can be ascribed to the presence of noncovalent interactions between the C–H moieties of the phenanthrene backbone and the electron-rich transition metal[44–46] as well as the alkynyl π-systems[30,47] (*cf.* also Fig. S3†). Notably, it can be derived that the two alkynyl–silver atoms in the BPE–Ag dimer (green cycles in Fig. 2b) tend to occupy a hexagonal close-packed (hcp) hollow site and a face-centred cubic (fcc) hollow site, respectively, with a well-defined distance of $d = 2\sqrt{7/3}\ a_0 = 8.83$ Å, and all the BPE–Ag dimers in the P1 phase follow the same adsorption configuration (*cf.* Fig. 2c). This typical feature was also observed for the other two phases. The preference of alkynyl–Ag atom residing on the hollow sites agrees well with the previous studies.[30,32,35]

For tiling analysis of the P1 phase, we define the centre of the building block as the vertex of the network, that is, the midpoint of the two alkynyl–Ag atoms in the BPE–Ag pair with well-defined registry (*cf.* white circles in Fig. 2b). After linking all the vertices in the network, an intriguing (3.6.3.6) tiling (Kagome) pattern emerges. Regular triangles and hexagons in Kagome tiling share the same edge with its length $b = \sqrt{61}\, a_0 = 22.56$ Å. In addition, if the three alkynyl–Ag atoms in the triangular tile are linked, a smaller regular triangle can be obtained (highlighted with green in Fig. 2c and d; $c = 2\sqrt{7}\, a_0 = 15.29$ Å), which is rotated 7.2° counter clockwise with respect to the former (Fig. 2b and d). Accordingly, the organizational chirality[48,49] of phase P1 can be defined and denoted by λ. Its enantiomorphic domain was also observed and denoted by ρ (*cf.* detailed discussions in ESI,† Fig. S4).

Kagome phase 2 (P2)

Fig. 3a depicts another long-range ordered supramolecular architecture denoted by P2. Likewise, we employed simple rod representation to examine the organizational

characteristics of BPE–Ag complexes in the network as an initial step. The main feature is again that the BPE–Ag species are paired. Moreover, it is clear to see that each nanopore is enclosed by six BPE–Ag monomers, leading to a smaller cavity (size ≈ 168.36 Å²) compared to that of the P1 phase. To determine the unit cell parameters for P2, two primitive translation vectors were constructed in the same manner as that employed for P1, and a statistical analysis of high-resolution STM images yielded $|\vec{a}'_{P2}| = 36.8 \pm 0.1$ Å, $|\vec{b}'_{P2}| = 36.7 \pm 0.1$ Å and $\alpha'_{P2} = 58.2 \pm 0.5°$. The angle γ'_{P2} between $\vec{b}'_{P2}$ and one of the [$\bar{1}$10] high-symmetry directions is 8.8 ± 0.1° (*cf.* Fig. 3b).

We transformed the experimental values into a commensurate superstructure model for the P2 phase (Fig. 3b), which has the matrix notation:

$$\begin{pmatrix} \vec{a}_{P2} \\ \vec{b}_{P2} \end{pmatrix} = \begin{pmatrix} 14 & 2 \\ -2 & 12 \end{pmatrix} \begin{pmatrix} \vec{u} \\ \vec{v} \end{pmatrix}.$$

The model gives $|\vec{a}_{P2}| = |\vec{b}_{P2}| = 2\sqrt{43}\, a_0 = 37.89$ Å, $\alpha_{P2} = 60°$ and $\gamma_{P2} = 7.6°$, which are comparable to the experimental
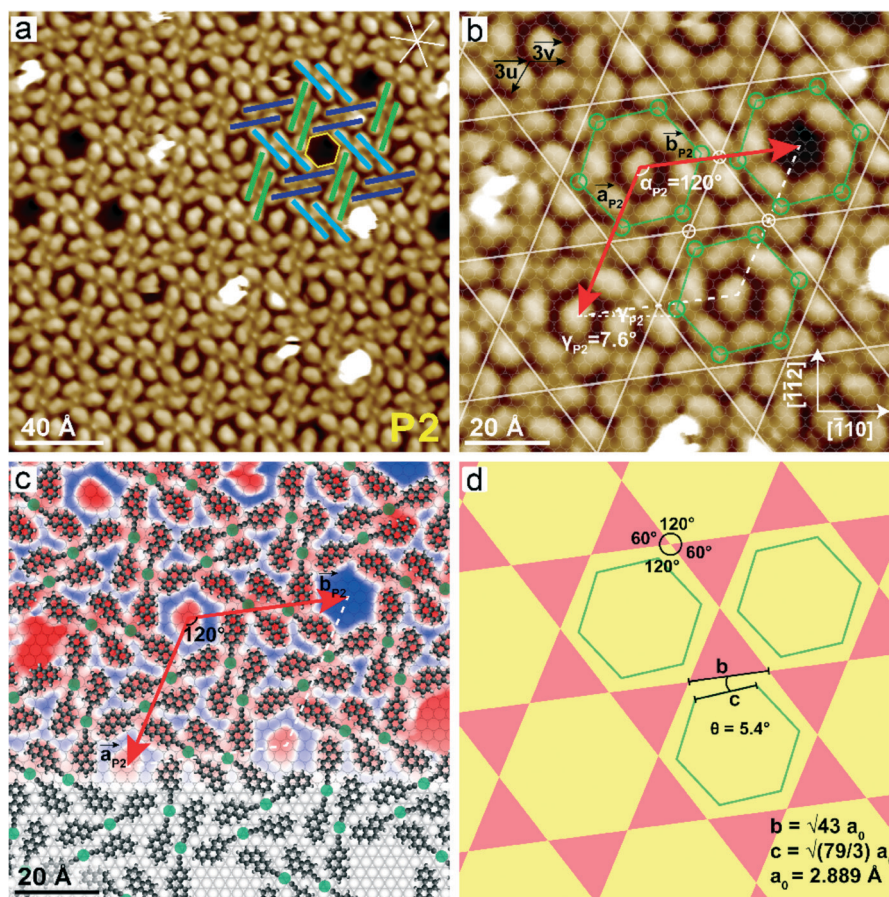

Fig. 3 Molecular-level expression of the P2 phase. (a) High-resolution STM image of λ-domain of P2. The coloured straight lines are used to represent BPE–Ag molecules with different in-plane orientations. The yellow hexagon highlights the nanopore enclosed by six BPE–Ag monomers. $I_t = 50$ pA, $U_s = 1.0$ V. (b) Magnified STM image of (a) with a commensurate unit cell model and proposed registry. Green and white circles highlight Ag-bis-acetylide nodes and the midpoints of the BPE–Ag pairs, respectively, and the Kagome (3.6.3.6) tiling is recognized. (c) STM image of (b) superimposed with molecular registry. (d) Tiling representation of (b) with geometric parameters.

values within an error smaller than 3.2%. For phase P2, each unit cell comprises 6 BPE–Ag complexes assuming an empty nanocage, and the molecular density of the P2 phase is calculated to be $\eta_{P2} = 0.97$ molecule per nm^2, which is higher than that of the P1 phase and is close to its starting EP coverage (~ 1.02 molecule per nm^2).

Applying the same procedure to extract the molecular adsorption registries, we also found that for the P2 phase, the alkynyl–Ag atoms in the BPE–Ag pairs (green cycles in Fig. 3b and c) adopt two different types of hollow sites with a fixed distance $d = 2\sqrt{7/3}\, a_0 = 8.83$ Å, same as that observed in the P1 phase. The tiling analysis was performed *via* linking all midpoints (white circles in Fig. 3b) in the BPE–Ag dimers in the network, and another (3.6.3.6) AT is clearly resolved (*cf.* Fig. 3b and d). The joint edge b between regular triangles and hexagons in this Kagome tiling has the length of 18.94 Å ($b = \sqrt{43}\, a_0$). Phase P2 also presents organization chirality. In this case, the alkynyl–Ag nodes in the hexagonal tile are linked, which gives rise to a smaller regular hexagon (highlighted in green in Fig. 3b and d; $c = \sqrt{79/3}\, a_0 = 14.83$

Å), rotating 5.4° counter-clockwise with respect to the larger hexagonal tile (*cf.* Fig. 3b and d). Accordingly, the domain depicted in Fig. 3 is labelled by λ and its opposite ρ-enantiomorphic counterpart is shown in the ESI† (Fig. S5).

The (3.4.6.4) AT phase (P3)

Finally, we discuss the third and the last porous phase (denoted by P3) experimentally found (Fig. 4a). In a similarly manner, paired BPE–Ag species were clearly resolved in the P3 phase using rod representation. Apart from the hexagonal cavity (size ≈ 168.36 Å^2) and the triangular nanopore, both enclosed by BPE–Ag units, a new type of nanopore surrounded by four BEP-Ag pairs exists in the network (illustrated by red rectangles in Fig. 4a). For the P3 phase, the two primitive translation vectors are also defined *via* linking adjacent hexagonal pore centres along two different directions (*cf.* Fig. 4b). The measured lengths of the vectors are $|\vec{a}'_{P3}| = 54.6 \pm 0.1$ Å, $|\vec{b}'_{P3}| = 54.6 \pm 0.4$ Å and $\alpha'_{P3} = 60.5 \pm 0.1°$. The angle γ'_{P3} between $\vec{b}'_{P3}$ and one of the [$\bar{1}$10] high-
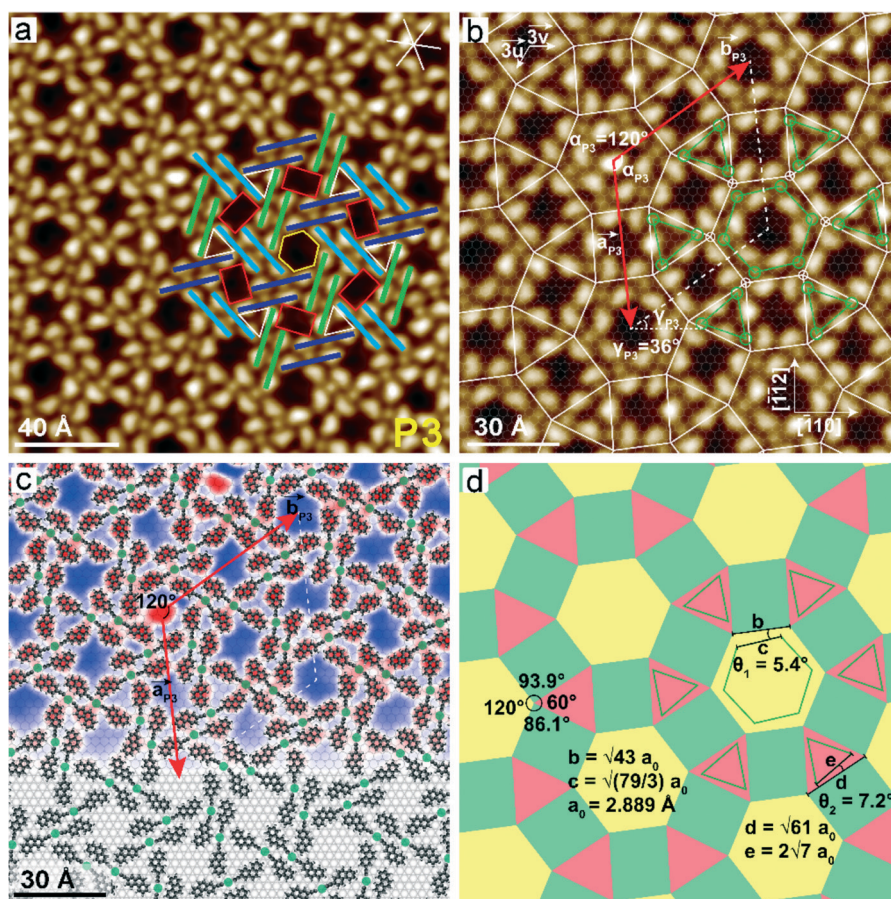

Fig. 4 The new (3.4.6.4) phase (P3) and its molecular-level expression. (a) High-resolution STM image of λ-domain of P3. The coloured straight bars represent BPE–Ag species with three different in-plane directions. The yellow hexagon, triangles and the red rectangles mark the nanopores enclosed by six BPE–Ag monomers, three monomers and four dimers, respectively. $I_t = 30$ pA, $U_s = 1.0$ V. (b) Magnified STM image of (a) with a commensurate unit cell model and proposed registry. Green circles highlight Ag-bis-acetylide nodes, whereas the white circles are the midpoints of the BPE–Ag pairs. Linking white circles gives rise to the (3.4.6.4) AT. (c) STM image of (b) superimposed with molecular models and registry. (d) Tiling representation of (b) with geometric parameters.

symmetry directions (horizontal direction in Fig. 4b) is 35.7 ± 0.3°. Based on the experimental values, a commensurate supercell can be inferred:

$$\begin{pmatrix} \vec{a}_{P3} \\ \vec{b}_{P3} \end{pmatrix} = \begin{pmatrix} 22 & 13 \\ -13 & 9 \end{pmatrix} \begin{pmatrix} \vec{u} \\ \vec{v} \end{pmatrix},$$

which corresponds to $|\vec{a}_{P3}| = |\vec{b}_{P3}| = \sqrt{367} \, a_0 = 55.35$ Å, $\alpha_{P3} = 60°$, and $\gamma_{P3} = 36°$ within an error of approximately 1.4%. Accordingly, the unit-cell size of phase P3 (≈ 2653 Å^2) amounts to nearly twice the size of the iodine-embedded one (≈ 1417 Å^2).[30] The elementary cell of the P3 phase contains 12 BPE–Ag units in total without counting the trapped molecules in the hexagonal or rectangular cages. The molecular density of the P3 phase is thus $\eta_{P3} = 0.90$ molecule per nm^2, which lies between that of the P1 and the P2 phases, and is slightly denser than the (3.4.6.4) AT (0.85 molecule per nm^2) obtained by employing EIP as the precursor.[30] The initial EP coverage required for generating P3 phase is around 0.86 molecule per nm^2.

Further analysis showed that the favourable adsorption registry of BPE–Ag dimer in P3 phase (green cycles in Fig. 4b and c) is the same as that of the other two phases. Accordingly, the mid positions of the BPE–Ag dimers are all linked to examine its tiling characteristics. Intriguingly, for the P3 phase three types of polygons including triangles, parallelograms and hexagons can be identified, and its tiling pattern mimics the (3.4.6.4) AT.[30] Further analysis (Fig. 4c) shows that the parallelogram in the (3.4.6.4) AT has different lengths for its two adjacent edges: $b = \sqrt{43} \, a_0 = 18.94$ Å (joined with a hexagon) and $d = \sqrt{61} \, a_0 = 22.56$ Å (joined with a triangle). The interior angles of the parallelogram can be determined from the tiling model as 86.1° and 93.9°, respectively (Fig. 4c), which are similar to those values derived from the iodine-incorporated (3.4.6.4) AT.[30] Likewise, the λ-enantiomorphic domain of this phase can be defined *via* linking the silver nodes in either the triangular or hexagonal tiles. Accordingly, both the smaller triangle ($c = \sqrt{79/3} \, a_0 = 14.83$ Å) and the hexagonal ($e = 2\sqrt{7} \, a_0 = 15.29$ Å) show a counter-clockwise rotating angle of 5.4° and 7.2°, respectively, with respect to their residing tiles (Fig. 4b and d). The experimentally observed enantiomorphic domain with opposite handedness is included in the ESI† (Fig. S6).

It is worth noting that both *cis* and *trans* BPE–Ag conformers exhibit in all three phases without apparent order. To gain further insight, we carried out statistical analysis on the geometrical configurations of BPE–Ag species in dimers (*cf.* Fig. S7†), which can be classified into three groups: concave paired, concave–convex paired, and convex paired. The statistics show that for all three phases, the concave pairing configurations prevail over the concave–convex pairing. Moreover, the convex paired BPE–Ag dimers are far more less encountered. Thus it can be inferred that the concave paired dimer is most energetically favourable.

The conformational flexibility exhibiting in the BPE–Ag species introduces local disorders[50] in each supramolecular phase. Nevertheless, the crystallinity of all three phases are not affected as certified by the sharp reciprocal spots[51] shown in 2D-FFT maps (*cf.* Fig. 1b–d).

Conclusions

To conclude, we verified in this study that O$_2$-gas exposure to a *de novo* synthesized alkyne derivative provides an effective terminal alkyne deprotonation process on Ag(111)/mica held at RT, affording organometallic BPE–Ag bis-acetylide species in high yield (>92%, *cf.* ESI†). Moreover, the spontaneously expressed alkynyl–Ag–alkynyl complexes represent versatile ingredients for organometallic networks, bearing promise for interesting functional properties such as optical nonlinearity, luminescence, and electrical conductivity.[52–56] Our results imply that O$_2$-mediated terminal alkyne deprotonation is likely a general reaction, the potential of which can be further developed *via* checking other types of metal surfaces as well as crystal facets. The BPE–Ag complexes realized in this study can express three distinct types of nanoporous phases by tuning the initial EP coverages. The basic tectons for all three phases are revealed to be BPE–Ag organometallic dimers, in which alkynyl–Ag atoms adopt the same registry. By defining the midpoint of the BPE–Ag pairs as the vertex of the networks, two nanoporous phases are found to be the semiregular Kagome tiling, whereas the third phase features the (3.4.6.4) AT. The new (3.4.6.4) AT is distinguished from the previously reported one by two correlated aspects: (i) iodine atoms are not incorporated or stabilizing the networks, (ii) basic units are BPE–Ag pairs instead of BPE–Ag monomers. Our results furthermore certify that complex tessellations can be systematically triggered *via* generating higher-level tectons through chemical transformation of simple molecular species. The current study also prepares the ground for electronic property investigations or surface state confinement and orbital character elucidation of the 2D supramolecular crystals, aiming at unravelling exotic electronic features of the semiregular ATs.

Methods

Samples preparation

Ag(111)/mica surfaces were prepared *in situ* under UHV conditions (base pressure < 4.0×10^{-10} mbar) by repeated cycles of Ar$^+$ sputtering, and annealing to ~620 K. The synthesis of ethynyl-phenanthrene (EP) molecules was reported earlier.[30] EP molecules were sublimated by an organic molecular beam epitaxy (OMBE) from quartz crucible at temperatures between 300 and 320 K onto Ag(111)/mica substrates (~300 K). Three different porous phases were prepared by an alkyne deprotonation procedure *via* introducing O$_2$ gas (≈ 6000 L) into the preparation chamber by backfilling through a leak valve.

STM experiments

The STM measurements were carried out in a homemade UHV LT-STM system (base pressure $< 3.0 \times 10^{-10}$ mbar). Tungsten tips were used for STM measurements. Morphology data were recorded at equilibrium temperatures of 4.5 K. The unit cell parameters were obtained by analysing images of the same area with four different slow scanning directions to minimize error due to drift. The unit cell orientation with respect to the substrate could be determined by directly resolving the substrate silver atoms.

DFT calculations

Cluster DFT calculations were performed with the ORCA quantum chemistry code.[57] Geometry optimization was done in the gas-phase with in-plane constraints and a revised Perdew, Burke, and Ernzerhof (RPBE)[58,59] exchange–correlation functional was employed along with the def2-SVP basis set.

Conflicts of interest

The authors declare no conflict of interest.

Acknowledgements

Notes and references

1 J. Kepler, *Harmonices Mundi (Johannes Planck)*, 1619.
2 B. Grünbaum and G. C. Shephard, *Mathematics Magazine*, 1977, **50**, 227–247.
3 D. Chavey, *Comput. Math. Appl.*, 1989, **17**, 147–165.
4 R. Mas-Ballesté, C. Gómez-Navarro, J. Gómez-Herrero and F. Zamora, *Nanoscale*, 2011, **3**, 20–30.
5 K. S. Novoselov, A. Mishchenko, A. Carvalho and A. H. Castro Neto, *Science*, 2016, **353**, aac9439.
6 H. Yao and S. A. Kivelson, *Phys. Rev. Lett.*, 2007, **99**, 247203.
7 E. Tang, J. W. Mei and X. G. Wen, *Phys. Rev. Lett.*, 2011, **106**, 236802.
8 X. Hu, M. Kargarian and G. A. Fiete, *Phys. Rev. B: Condens. Matter Mater. Phys.*, 2011, **84**, 155116.
9 D. J. J. Farnell, O. Götze, J. Richter, R. F. Bishop and P. H. Y. Li, *Phys. Rev. B: Condens. Matter Mater. Phys.*, 2014, **89**, 184407.
10 J. A. Millan, D. Ortiz, G. van Anders and S. C. Glotzer, *ACS Nano*, 2014, **8**, 2918–2928.
11 M. A. Springer, T. J. Liu, A. Kuc and T. Heine, *Chem. Soc. Rev.*, 2020, **49**, 2007–2019.
12 S. Thomas, H. Li, R. R. Dasari, A. M. Evans, I. Castano, T. G. Allen, O. G. Reid, G. Rumbles, W. R. Dichtel, N. C. Gianneschi, S. R. Marder, V. Coropceanu and B. Jean-Luc, *Mater. Horiz.*, 2019, **6**, 1868–1876.
13 S. Thomas, H. Li, C. Zhong, M. Matsumoto, W. R. Dichtel and J.-L. Bredas, *Chem. Mater.*, 2019, **31**, 3051–3065.
14 F. C. de Lima, G. J. Ferreira and R. H. Miwa, *Phys. Chem. Chem. Phys.*, 2019, **21**, 22344–22350.
15 W. Jiang, X. Ni and F. Liu, *Acc. Chem. Res.*, 2021, **54**, 416–426.
16 Z. Lin, J.-H. Choi, Q. Zhang, W. Qin, S. Yi, P. Wang, L. Li, Y. Wang, H. Zhang, Z. Sun, L. Wei, S. Zhang, T. Guo, Q. Lu, J.-H. Cho, C. Zeng and Z. Zhang, *Phys. Rev. Lett.*, 2018, **121**, 096401.
17 J.-X. Yin, S. S. Zhang, G. Chang, Q. Wang, S. S. Tsirkin, Z. Guguchia, B. Lian, H. Zhou, K. Jiang, I. Belopolski, N. Shumiya, D. Multer, M. Litskevich, T. A. Cochran, H. Lin, Z. Wang, T. Neupert, S. Jia, H. Lei and M. Z. Hasan, *Nat. Phys.*, 2019, **15**, 443–448.
18 J.-M. Lehn, *Supramolecular chemistry: Concepts and perspectives*, VCH, Weinheim, 1995.
19 B. Moulton and M. J. Zaworotko, *Chem. Rev.*, 2001, **101**, 1629–1658.
20 J. V. Barth, G. Costantini and K. Kern, *Nature*, 2005, **437**, 671–679.
21 J. V. Barth, *Annu. Rev. Phys. Chem.*, 2007, **58**, 375–407.
22 U. Schlickum, R. Decker, F. Klappenberger, G. Zoppellaro, S. Klyatskaya, W. Auwärter, S. Neppl, K. Kern, H. Brune, M. Ruben and J. V. Barth, *J. Am. Chem. Soc.*, 2008, **130**, 11778–11782.
23 Z. Shi and N. Lin, *J. Am. Chem. Soc.*, 2009, **131**, 5376.
24 D. Ecija, J. I. Urgel, A. C. Papageorgiou, S. Joshi, W. Auwärter, A. P. Seitsonen, S. Klyatskaya, M. Ruben, S. Fischer, S. Vijayaraghavan, J. Reichert and J. V. Barth, *Proc. Natl. Acad. Sci. U. S. A.*, 2013, **110**, 6678–6681.
25 J. I. Urgel, D. Ecija, W. Auwärter, A. C. Papageorgiou, A. P. Seitsonen, S. Vijayaraghavan, S. Joshi, S. Fischer, J. Reichert and J. V. Barth, *J. Phys. Chem. C*, 2014, **118**, 12908–12915.
26 G. Lyu, Q. Zhang, J. I. Urgel, G. Kuang, W. Auwärter, D. Ecija, J. V. Barth and N. Lin, *Chem. Commun.*, 2016, **52**, 1618–1621.
27 P. A. Held, H. Fuchs and A. Studer, *Chem. – Eur. J.*, 2017, **23**, 5874–5892.
28 S. Clair and D. G. de Oteyza, *Chem. Rev.*, 2019, **119**, 4717–4776.
29 L. Grill and S. Hecht, *Nat. Chem.*, 2020, **12**, 115–130.
30 Y.-Q. Zhang, M. Paszkiewicz, P. Du, L. Zhang, T. Lin, Z. Chen, S. Klyatskaya, M. Ruben, A. P. Seitsonen, J. V. Barth and F. Klappenberger, *Nat. Chem.*, 2018, **10**, 296–304.
31 F. Klappenberger, Y.-Q. Zhang, J. Björk, S. Klyatskaya, M. Ruben and J. V. Barth, *Acc. Chem. Res.*, 2015, **48**, 2140–2150.
32 Y.-Q. Zhang, T. Paintner, R. Hellwig, F. Haag, F. Allegretti, P. Feulner, S. Klyatskaya, M. Ruben, A. P. Seitsonen, J. V. Barth and F. Klappenberger, *J. Am. Chem. Soc.*, 2019, **141**, 5087–5091.

33 Q. Sun, L. Cai, H. Ma, C. Yuan and W. Xu, *ACS Nano*, 2016, **10**, 7023–7030.

34 Z. Yang, J. Gebhardt, T. A. Schaub, T. Sander, J. Schönamsgruber, H. Soni, A. Görling, M. Kivala and S. Maier, *Nanoscale*, 2018, **10**, 3769–3776.

35 J. Liu, Q. Chen, K. Cai, J. Li, Y. Li, X. Yang, Y. Zhang, Y. Wang, H. Tang and D. Zhao, *Nat. Commun.*, 2019, **10**, 1–10.

36 Z. Yang, T. Sander, J. Gebhardt, T. A. Schaub, J. R. Schönamsgruber, H. R. Soni, A. Görling, M. Kivala and S. Maier, *ACS Nano*, 2020, **14**, 16887–16896.

37 C.-H. Shu, Y. He, R.-X. Zhang, J.-L. Chen, A. Wang and P.-N. Liu, *J. Am. Chem. Soc.*, 2020, **142**, 16579–16586.

38 N. Kepčija, Y.-Q. Zhang, M. Kleinschrodt, J. Björk, S. Klyatskaya, F. Klappenberger, M. Ruben and J. V. Barth, *J. Phys. Chem. C*, 2013, **117**, 3987–3995.

39 Y.-Q. Zhang, T. Lin, B. Cirera, R. Hellwig, C.-A. Palma, Z. Chen, M. Ruben, J. V. Barth and F. Klappenberger, *Angew. Chem., Int. Ed.*, 2017, **56**, 7797–7802.

40 M. Nishio, *CrystEngComm*, 2004, **6**, 130–158.

41 B. V. Andryushechkin, V. M. Shevlyuga, T. V. Pavlova, G. M. Zhidomirov and K. N. Eltsov, *Phys. Rev. Lett.*, 2016, **117**, 056101.

42 J. Pal, T. B. Rawal, M. Smerieri, S. Hong, M. Alatalo, L. Savio, L. Vattuone, T. S. Rahman and M. Rocca, *Phys. Rev. Lett.*, 2017, **118**, 226101.

43 L. Merz and K.-H. Ernst, *Surf. Sci.*, 2010, **604**, 1049–1054.

44 L. Brammer, D. Zhao, F. T. Ladipo and J. Braddock-Wilking, *Acta Crystallogr., Sect. B: Struct. Sci., Cryst. Eng. Mater.*, 1995, **51**, 632–640.

45 D. Braga, F. Grepioni and G. R. Desiraju, *Chem. Rev.*, 1998, **98**, 1375–1406.

46 T. Steiner, *Angew. Chem., Int. Ed.*, 2002, **41**, 48–76.

47 Y.-Q. Zhang, J. Björk, P. Weber, R. Hellwig, K. Diller, A. C. Papageorgiou, S. C. Oh, S. Fischer, F. Allegretti, S. Klyatskaya, M. Ruben, J. V. Barth and F. Klappenberger, *J. Phys. Chem. C*, 2015, **119**, 9669.

48 R. Raval, *Chem. Soc. Rev.*, 2009, **38**, 707–721.

49 K. H. Ernst, *Phys. Status Solidi B*, 2012, **249**, 2057–2088.

50 D. Ecija, S. Vijayaraghavan, W. Auwärter, S. Joshi, K. Seufert, C. Aurisicchio, D. Bonifazi and J. V. Barth, *ACS Nano*, 2012, **6**, 4258–4265.

51 *Acta Crystallogr., Sect. A: Found. Crystallogr.*, 1992, **48**, 922–946.

52 N. J. Long and C. K. Williams, *Angew. Chem., Int. Ed.*, 2003, **42**, 2586–2617.

53 C. E. Powell and M. G. Humphrey, *Coord. Chem. Rev.*, 2004, **248**, 725–756.

54 W.-Y. Wong, X.-Z. Wang, Z. He, A. B. Djurisic, C.-T. Yip, K.-Y. Cheung, H. Wang, C. S. K. Mak and W.-K. Chan, *Nat. Mater.*, 2007, **6**, 521–527.

55 W.-Y. Wong and P. D. Harvey, *Macromol. Rapid Commun.*, 2010, **31**, 671–713.

56 L. Xu, J. Sun, T. Tang, H. Zhang, M. Sun, J. Zhang, J. Li, B. Huang, Z. Wang, Z. Xie and W.-Y. Wong, *Angew. Chem., Int. Ed.*, 2021, **60**, 11326–11334.

57 F. Neese, *WIREs Comput. Mol. Sci.*, 2012, **2**, 73–78.

58 J. P. Perdew, K. Burke and M. Ernzerhof, *Phys. Rev. Lett.*, 1996, **77**, 3865–3868.

59 B. Hammer, L. B. Hansen and J. K. Nørskov, *Phys. Rev. B: Condens. Matter Mater. Phys.*, 1999, **59**, 7413–7421.